

Inter- and intragrain currents in bulk melt-grown YBaCuO rings

A. B. Surzhenko,* M. Zeisberger, T. Habisreuther, and W. Gawalek
Institut für Physikalische Hochtechnologie, Winzerlaer Str. 10, Jena D-07745, Germany

L. S. Uspenskaya
*Institute of Solid State Physics, Russian Academy of Science,
 Institutskii pr. 16, Chernogolovka, Moscow district, 142432, Russia*
 (Dated: February 7, 2020)

A simple contactless method suitable to discern between the intergrain (circular) current, which flows in the thin superconducting ring, and the intragrain current, which does not cross the weakest link, has been proposed. At first, we show that the intergrain current may directly be estimated from the magnetic flux density $B(\pm z_0)$ measured by the Hall sensor positioned in the special points $\pm z_0$ above/below the ring center. The experimental and the numerical techniques to determine the value z_0 are discussed. Being very promising for characterization of a current flowing across the joints in welded YBaCuO rings (its dependencies on the temperature and the external magnetic field as well as the time dissipation), the approach has been applied to study corresponding properties of the intra- and intergrain currents flowing across the a -twisted grain boundaries which are frequent in bulk melt-textured YBaCuO samples. We present experimental data related to the flux penetration inside a bore of MT YBaCuO rings both in the non-magnetized, virgin state and during the field reversal. The shielding properties and their dependence on external magnetic fields are also studied. Besides, we consider the flux creep effects and their influence on the current re-distribution during a dwell.

PACS numbers: 74.72.Bk, 74.80.Bj, 74.60.Jg, 74.25.Ha

I. INTRODUCTION

Unique feature of thin superconducting rings has to be well-known to everybody who ever tried to investigate the intergrain (transport) currents flowing across weak links in polycrystalline $\text{YBa}_2\text{Cu}_3\text{O}_{7-\delta}$ (YBCO) ceramics and/or thin films^{1,2,3,4}. By changing the outer R_o and the inner R_i radii of the ring, one may essentially enlarge a difference between the length scales, $R_o + R_i$ and $R_o - R_i$, over which, respectively, the inter- and the intra-grain currents flow. Provided that the ring is thin enough ($R_o - R_i \ll (R_o + R_i)$), one may reliably register the magnetic flux density B induced by the intergrain, shielding current even if the intragrain currents much exceed it.

The melt-textured (MT) growing process⁵ has generally allowed to escape an appearance of the large-angle grain boundaries (GBs) and, thereby, the current localization inside the grains. For this reason, a worldwide interest to the ring-like geometry was fading away until an idea to weld⁶ MT blocks gained a respectable reputation^{7,8,9,10,11,12,13,14,15,16,17,18,19,20}. Briefly, the joining procedures consist in welding of single MT domains during a liquid-assisted process which either releases residual BaCuO-oxide trapped in the MT material⁸ or uses corresponding REBCO (RE=Tm^{9,10,11}, Yb^{12,16}, Er^{15,17}, Y^{7,20} or Y+Ag^{13,14,18}) compounds melting at lower temperatures. Since these techniques were shown to produce the joints capable to carry high currents, such artificial joining opens new perspectives for fabrication of large-scale superconducting devices (e.g., magnetic bearings, electromotors and generators, energy storage systems, *etc.*²¹). Their performance, through, crucially depends

on the density j_w of the critical current which the weld may transmit.

Despite of an obvious necessity to compare the joints obtained under different welding conditions, surprisingly few authors reported numerical values j_w . Besides, most of these estimates was obtained by the resistive measurements which, because of the ohmic losses in the current pads, are severely limited by the maximum admissible current $I_w = j_w S \lesssim 10^3 \text{ A}$. Thus, these measurements are restricted both by the surface S of the weld and by its quality j_w which, in turn, imposes the lowest temperature margin. On the other hand, prevalent contactless methods (e.g., levitation force technique^{9,19}, magneto-optical image analysis^{9,17,22}, the scanning Hall-sensor magnetometry^{8,9,10,11,12,13,14,15} and magnetization loop studies^{8,9,18}) are not free of ambiguities in processing of experimental data unless, as mentioned above, the welded sample has a shape of thin ring. In this case, the transport current throughout a ring is limited by the weakest link which is, in turn, usually associated with a joint.

Among the mentioned above experimental techniques, the scanning Hall sensor magnetometry looks preferable. The main reason is that, having no restrictions for a size of joints, this method is quite suitable for characterization of large-scale welds required for practical applications. The same feature seems also useful for other tasks to be eventually resolved. In particular, one has to study a degradation of transport currents from a center of large MT domains to their rims²⁴ and its relation to a content of the precursor mixture, the growth temperature, *etc.* Aside from a knowledge of the best growth conditions, such studies will allow to determine the op-

timum size of welded parts. The last, but not the least argument is a widespread use of the scanning Hall sensor systems^{8,9,10,11,12,13,14,15}.

For this technique to give reliable results, the experimental data have to be properly processed. Meanwhile, most of the authors prefer to simplify the genuine distribution of currents and to consider their rings as *homogeneous* (one-turn) solenoids carrying the transport current I_w . In other words, they neglect the intragrain currents, i.e. those which do not cross the joint. We shall hereafter demonstrate that such simplification is applicable only for rough estimates. More accurate method, i.e. a scan of the flux trapped by a ring with its subsequent computer fit¹⁰, is also far from perfect. The problem is that a necessity to move the Hall sensor makes this technique hard to exploit at different temperatures and/or external magnetic fields. Moreover, the scanning duration t_{sc} of, typically, a few minutes during which the currents may noticeably dissipate, assents to start the measurements only after a long-continued dwell $t_{dw} \gg t_{sc}$. So, an important information about the transport current losses appears unavailable.

Section II of this manuscript represents simple analytical equations constituting a backbone of the novel experimental approach which combines the advantages of both methods and is free of their faults. We show that to find out the densities of the inter- and the intragrain currents one does not need to waste a time on the magnetic flux scan. Actually, these densities may, with a proper accuracy, be estimated from two experimental points $B(r, z)$ measured at certain distances z above/below the ring center. In Section IV we apply this method to study the current distribution in the large-scale MT YBCO rings. The results are summarized in Section V.

II. MODEL AND ITS SOLUTION

Let us consider a homogeneous ring (see Fig. 1) made of superconducting material with the critical current density j_m and introduce therein a weak link transmitting a current up to

$$I_w = j_w(R_o - R_i)2L = j_m f(R_o - R_i)2L \quad (1)$$

where $f = j_w/j_m < 1$. It is worth of mentioning that the weak link makes this ring *inhomogeneous* with respect to a rotation around its axis, z . Let the ring was

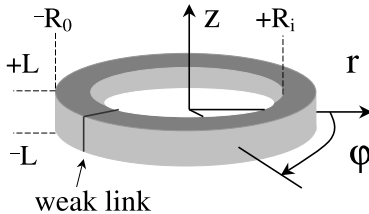


FIG. 1: Superconducting ring which contains weak link.

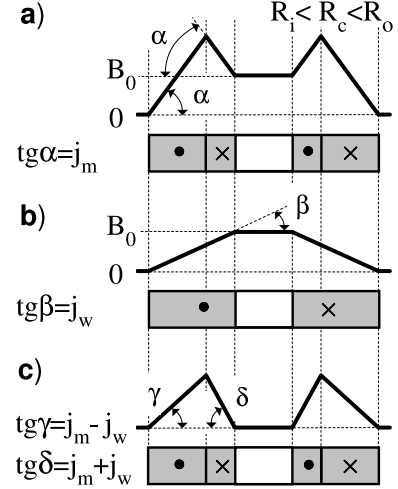


FIG. 2: Profiles of the density B of the remanent magnetic flux trapped by a ring containing weak links a) and its components, B_w and B_m , induced by b) the inter- and c) the intragrain currents, respectively.

completely magnetized in strong magnetic fields applied along the z -direction. The subject of our interest will be the currents flowing in the ring as well as the radial profiles $B(z = \text{Const}, r)$ of the magnetic flux density which these currents produce.

Assuming the Bean's critical state model to be valid, one can readily outline the profile passing through the point $r = 0$ and the ring area which is far enough from the weak link. Fig. 2a shows this profile for a semi-infinite ring $L \rightarrow \infty$ in the remanent state ($H = 0$). Of necessity, this situation can readily be expanded to the case of arbitrary fields by adding a constant background $\mu_0 H$. For this reason, we shall thenceforward take into account only two components of the magnetic flux, B_w and B_m . These are induced by the inter- (I_w) and the intragrain (I_m) currents which, respectively, crosses and does not cross the weak link. The former results to the triangle profile truncated in the ring bore by a plateau $B_0 = j_w(R_o - R_i)$ (Fig. 2b), whereas the latter responds for the difference $B_m = B - B_w$ (see Fig. 2c). The radius R_c wherein the intragrain current alters its direction from the clockwise (CW) to the counterclockwise (CCW) is known

$$R_c(f) = [R_o + R_i - f(R_o - R_i)]/2 \quad (2)$$

to change between $(R_i + R_o)/2$ at $f = 0$ and R_i ($f = 1$)¹⁰. Using Eq. (2), one can readily calculate the amplitude

$$I_m = j_m(R_o - R_i)L(1 - f^2) \quad (3)$$

and demonstrate that the CW and CCW intragrain currents compensate each another, i.e. the current loop I_m does appear closed inside the superconducting grain.

In the case $L \gg R_o$ shown in Fig. 2, $B_m(r < R_i) \equiv 0$, i.e. any point inside the ring bore is quite suitable to estimate the density $j_w = B_0/(R_o - R_i)$. This comfortable situation is, through, too far from reality. Since the

finite-height rings are not free of demagnetizing effects, the term $B_m(r < R_i)$ is actually non-zero. Thus, in order to estimate the current I_w and/or its density j_w , one has to calculate and to remove the component B_m from the experimentally accessible value $B(z, r)$. In this paper we follow a bit another way. We show and gladly exploit that $B_m(z, r)$ is an alternating function: it is negative inside a certain region surrounding the ring center ($z = 0, r = 0$) and positive outside it (see, for example, Fig. 3a). Thus, positioning the Hall sensor somewhere at the border $B_m(z_0, r_0) = 0$, one can directly measure the flux component $B_w(z_0, r_0)$ and use this value to restore a “pure” transport current flowing throughout a ring.

One could, certainly, search for a whole surface which satisfy the condition $B_m(z_0, r_0) = 0$. But let, for simplicity, restrict our search by the points along the ring axis, $r_0 = 0$. The magnetic flux density of the infinitely thin ($R_i = R_o = R$), one-turn solenoid at $r = 0$ is well-known

$$B = \frac{I}{4L} \left[\frac{L - z}{\sqrt{R^2 + (L - z)^2}} + \frac{L + z}{\sqrt{R^2 + (L + z)^2}} \right]. \quad (4)$$

More general case ($R_i \neq R_o$) requires to average the function given by Eq. (4) over the range between the outer r_o and the inner r_i radii. Using a formal averaging procedure $B = \int B(R) dR / \int dR$, one has a solution for thick superconducting rings

$$B = j \cdot \Phi(L, z, r_o, r_i). \quad (5)$$

Here j denotes the current density $j = I/[2L(r_o - r_i)]$ and the function Φ gives the effective size depending on four distances

$$\begin{aligned} \Phi(L, z, r_o, r_i) &= \Gamma(L - z, r_o, r_i) + \Gamma(L + z, r_o, r_i), \\ \Gamma(x, r_o, r_i) &= \frac{x}{2} \ln \left(\frac{r_o + \sqrt{r_o^2 + x^2}}{r_i + \sqrt{r_i^2 + x^2}} \right). \end{aligned} \quad (6)$$

Using these equations, we can obtain the magnetic flux densities, B , B_w and B_m , produced by each of three magnetic systems shown in Figs. 2a–c. The whole ring (see Fig. 2a), for example, corresponds to a pair of solenoids having the same height $2L$ and the common radius R_c given by Eq. (2). Since within the critical state model the slope α is definitely equal to j_m , such magnetic pair induces the flux density

$$B = j_m [\Phi(L, z, R_o, R_c(f)) - \Phi(L, z, R_c(f), R_i)]. \quad (7)$$

Using similar arguments, one can write for the coil carrying the transport current I_w (Fig. 2b)

$$B_w = j_w \Phi(L, z, R_o, R_i) \quad (8)$$

and readily calculate the remainder $B_m = B - B_w$

$$\begin{aligned} B_m &= j_m [(1 - f)\Phi(L, z, R_o, R_c(f)) - \\ &\quad - (1 + f)\Phi(L, z, R_c(f), R_i)] \end{aligned} \quad (9)$$

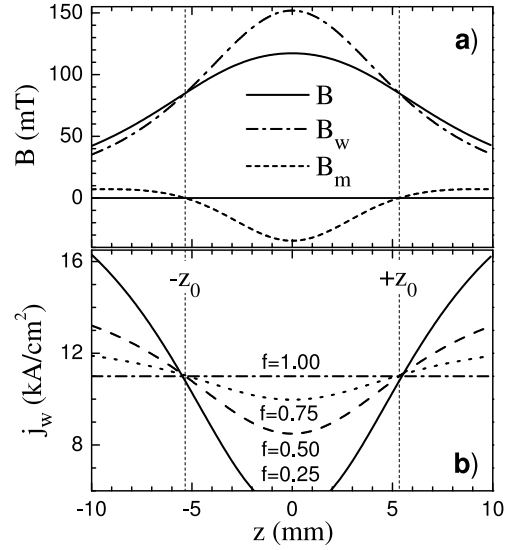


FIG. 3: Figure a) shows how the densities of the remanent magnetic flux B and its components, B_w and B_m , along the axis ($r = 0$) of the ring depend on the distance z from its center, $z = 0$. The ring sizes, $R_o = 10 \text{ mm}$, $R_i = 5.5 \text{ mm}$, $2L = 3.8 \text{ mm}$, as well as $j_w = 11 \text{ kA/cm}^2$ are borrowed from the work of Zheng *et al.*¹⁰. The missing parameter $f = j_w/j_m$ is taken to be $f = 0.5$ ($j_m = 22 \text{ kA/cm}^2$). The j_w vs z curves in figure b) are calculated from the total magnetic flux B within the one-turn approximation (8) and, thus, represent an error appearing when the term B_m is neglected.

generated by the intragrain current loop (Fig. 2c).

To imagine how the flux densities (7)–(9) change along the ring axis, we inserted parameters of the real ring reported in Ref. 10 to Eqs. (7)–(9) and presented these curves in Fig. 3a. These data once more convince us that the one-turn approximation (8) may properly be applied to experimental values $B(z)$ only when $B_m = 0$, i.e. at the points $z_0 \approx \pm 5.4 \text{ mm}$ on the given axis ($r = 0$). Otherwise, such method may considerably underestimate ($|z| < z_0$) or overestimate ($|z| > z_0$) the current density j_w . For the parameter $f = 0.5$ in Fig. 3a, the j_w value, respectively of the Hall sensor position $0 \leq |z| \leq 10 \text{ mm}$, changes in the wide range (77...120%) around the genuine density $j_w = 11 \text{ kA/cm}^2$. This error essentially increases when $f \rightarrow 0$ (see Fig. 3b).

To escape such situation, one has to derive z_0 . The main problem, which will encounter everybody trying to do it, is that the expression inside the brackets in Eq. (9) depends on the unknown factor $f = j_w/j_m$ and so, certainly, does z_0 which satisfies

$$\frac{\Phi(L, z_0, R_o, R_c(f))}{\Phi(L, z_0, R_c(f), R_i)} = \frac{1 + f}{1 - f}. \quad (10)$$

If one could ignore this dependence, z_0 would be defined only by the ring geometry and, hence, readily calculated.

Upon a closer view at Fig. 3b, one can really note that z_0 tends to the ring center as f increases. However, the effect seems so weak that we did not resist a temptation

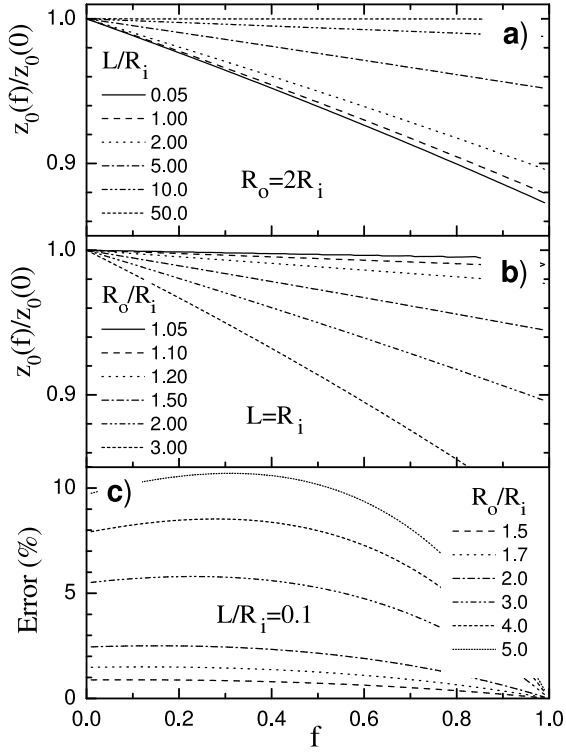


FIG. 4: a), b) The z_0 vs f dependencies calculated from Eq.(10) at various parameters R_o , R_i and L . Figure c) presents the error $B_m/B_w(z_0)$ which appear in the worse case of thick, flat rings ($R_o/R_i > 1.5$, $L/R_i = 0.1$) provided that the z_0 vs f dependence is neglected, namely, $z_0(f) = z_0(0)$.

to know in which rings its disregard still gives an acceptable error. We studied the z_0 vs f curves at various parameters R_o , R_i and $2L$ and revealed almost no deviation from the initial value $z_0(f=0)$ in thin ($R_i \rightarrow R_o$) and/or high ($L \rightarrow \infty$) rings (see Fig. 4a,b), i.e. in those which are close to a form of ideal solenoid. As the largest deviation is, therefore, expected in thick, flat rings ($R_o \gg R_i$, $L \ll R_i$), it is the case to be inspected. So, we calculated for such rings the amendment $B_m/B_w|_{z_0}$ which has, by the definition, to be a zero unless the z_0 vs f dependence is ignored. The points $z_0(R_i, R_o, L) = \text{Const}$, wherein this ratio was estimated, were taken from Eq. (10) reduced by the substitution $f = 0$ to rather comfortable form³⁷

$$\Phi(L, z_0, R_o, R_c(0)) = \Phi(L, z_0, R_c(0), R_i), \quad (11)$$

where $R_c(0) = (R_o + R_i)/2$. Accepting the admissible error to be 2.5% and restricting, thereby (see Fig. 4c), the studied rings by not too stringent condition³⁸ $R_o/R_i \leq 2$, we are qualified to use the above simplification, $z_0(f) = z_0(0)$, in practice.

Thus, knowing the ring sizes (R_o , R_i and $2L$) only, one may, on the one hand, pre-determine z_0 from Eq. (11) by numerical methods. Such solutions (normalized, for the sake of convenience, to the ring half-height L) are shown in Fig. 5. On the other hand, this numerical procedure

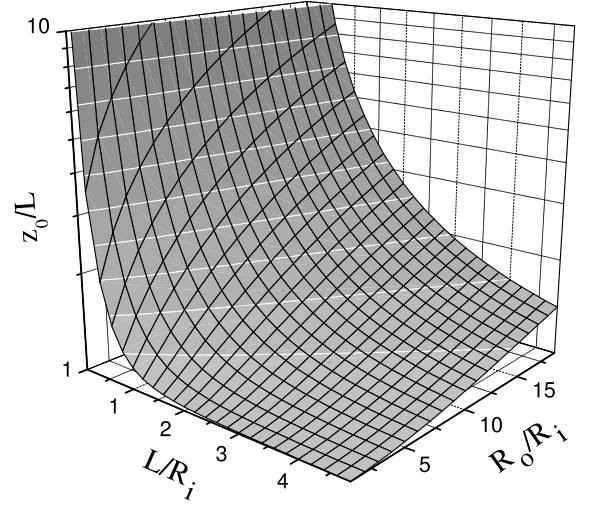


FIG. 5: The solutions of Eq. (11) normalized to the ring half-height. Note that everywhere, except for the case of an ideal solenoid ($L \rightarrow \infty$, $R_o/R_i \rightarrow 1$), z_0 appears outside of the ring, $|z_0| \geq L$. Thus, the method is not restricted by the bore diameter $2R_i$ which may be smaller than the size of the Hall sensor holder.

(at least, in the case of welded rings) may *optionally* be avoided. Before joining, these rings inevitably contain one or more slits which prevent a transport current to flow ($f = 0$). So, the points $\pm z_0$, wherein the remanent flux density of the *cut* ring changes its sign (see Fig. 3a), are available for direct measurements. Then, registering $B(\pm z_0)$ above or below the center of the *welded* sample, one may readily calculate the joint quality

$$j_w = B(z_0)/\Phi(L, z_0, R_o, R_i). \quad (12)$$

Since z_0 depends only on the ring geometry, there is no matter whether the welded ring has the same j_m as that in the original material or not. This feature does look important because heating of the MT samples up to temperatures close to their melting points, which actually is the joining procedure, often results to the oxygen losses and requires to re-oxygenate the samples.

III. EXPERIMENTAL DETAILS

The initial MT YBCO samples, from which we cut the rings, were grown by the top-seeding method which is described in details elsewhere²⁵. Briefly, commercially purchased powders of $\text{YBa}_2\text{Cu}_3\text{O}_{7-\delta}$ and Y_2O_3 were thoroughly mixed in proportions providing the final phase composition $\text{Y}:\text{Ba}:\text{Cu}=1.5:2:3$ and diluted by 1 wt.% CeO_2 . This mixture was uniaxially pressed into cylindrical pellets which sizes were selected to exceed the sizes of future rings. Then, the self-made $\text{SmBa}_2\text{Cu}_3\text{O}_X$ seed was installed in the center of each pellet and oriented so that its crystallographic axis c , $[001]$, was parallel to the axis of cylinder. On the morrow of isothermal melt-growth ($T = 988^\circ\text{C}$) the samples were cooled down to

the room temperature and then post-annealed in flowing oxygen.

The rings were carved (by using the aluminium oxide grindstones) so that the z -axis of each ring was parallel to the c -axis of the initial MT crystal.

The larger half of experiments was in scanning of the *remanent* flux distribution. These scans were performed with the 3D-positioning system²⁶ allowing to move the Hall sensor stepwise with a pitch of $100\mu m$ in the horizontal plane and of $75\mu m$ along the vertical direction. The standard procedure was the following. The rings were mounted inside a small vessel and field-cooled (FC) in magnetic fields $\mu_0 H \approx 1 T$ to the liquid nitrogen temperature $T = 77.3 K$. Then, the field was switched off (with a sweep rate $0.5 T/min$) and a ring (still inside a vessel with a liquid nitrogen) was moved to an area available for a scan. To eliminate the undesirable scatter because of a dissipation of the remanent flux during the scanning time (typically, of a few minutes), a scan was always run after a long-continued dwell ($t_{dw} = 30 min$). Both the axial $B(r = 0, z)$ and the radial $B(r, z = Const)$ profiles were studied.

To measure the hysteresis loops $B(H)$ as well as the flux dissipation $B(t)$, we mounted the Hall sensor directly on the studied ring. The Hall sensor positioning error did not exceed $50\mu m$.

The magnetic moment, m , was registered by the commercial VSM (Model No. 3001, Oxford Instruments Ltd). Owing to a relatively large distance between the vibrating ring and the pick-up coils, this value may roughly be associated with $B(z = \infty)$.

The radial flux distribution at the ring edges $z = \pm L$ in small magnetic fields ($H < 3 kOe$) was also visualized by using a high-resolution magneto-optical imaging technique²⁷.

IV. RESULTS AND DISCUSSION

In this section we report extensive experimental studies of the inter- and the intragrain currents for the ring-like geometry. At first, we investigate the current distribution in the remanent state and compare our results with those obtained by conventional methods. Then, we study a behavior of rings containing natural weak links (i.e. the boundaries between the a -twisted grains) in external magnetic fields. Finally, we explore the flux creep effects.

A. Cut rings in the remanent state

It is obvious that the fewer fitting parameters are included in an equation, the more trustworthy one can test whether it fits an experiment or not. For this reason, we start our studies from the cut rings wherein relevant is the only parameter, j_m .

When a ring contains one or more slits and transmits, hence, no transport current, the magnetic flux density along the ring axis ($r = 0$) is given by Eq. (9) at $f = 0$

$$B = j_m [\Phi(L, z, R_o, R_c(0)) - \Phi(L, z, R_c(0), R_i)], \quad (13)$$

where $R_c(0)$ is just the average radius, $(R_o + R_i)/2$ (see Eq. (2)). One has to note that the term in brackets totally defines the shape of the B vs z curve, i.e. j_m may change only its amplitude. Thus, estimating a disagreement between theoretical and experimental profiles $B(r = 0, z)$, one can readily check to what extent may our approach be relied on. In particular, one can put the solutions z_0 of Eq. (11) to the experimental proof. By changing the ring sizes, we can also test how j_m varies with a distance from the seeding point both in the axial and in the radial directions.

For these studies we used the ring (see Table I) which was cut from the central part of the MT crystal, i.e. the ring center ($r = 0$) coincided with the seeding point. The inner diameter, $2R_i = 5.90 mm$, was selected to exceed the size ($\approx 5 mm$) of the Hall sensor holder and to make, therefore, the ring suitable for the z -scan along the whole axis $r = 0$. At first, we cut this ring onto two 180° -arcs and glued them together by using an epoxy resin. A toughness of such mechanical contact was good enough for a succeeding treatment of the ring by grindstones. Then, grinding, step-by-step, the ring bottom (i.e. reducing the ring height), we measured at each stage the axial profile $B(r = 0, z)$ of the remanent flux density. During the measurements we exactly followed the procedure described in Section III. Some of these data are presented in Fig. 6 (open symbols). To calculate j_m and to recover from Eq. (13) theoretical approximations (solid curves), we used the B -points nearby the ring center, $z = 0$, wherein the flux density has the maximum amplitude. Fig. 6 shows that Eq. (13) well fits the experimental data. However, more careful look (see Table I)

TABLE I: Theoretical and experimental values z_0 in the cut rings (CR) of various sizes. Experimental estimates for the intragrain current density j_m are also included.

Ring No.	Ring sizes ^a , mm			z_0 , mm		j_m ^b ,
	R_o	R_i	$2L$	theory	exp.	kA/cm^2
CR1	6.05	2.95	5.35	3.92	3.70	16.0 ₁
CR2	"	"	4.90	3.83	3.67	16.9 ₀
CR3	"	"	3.98	3.60	3.52	18.0 ₁
CR4	"	"	3.30	3.46	3.40	19.0 ₀
CR5	"	"	2.81	3.37	3.34	20.1 ₄
CR6	"	"	2.22	3.27	3.23	20.3 ₃
CR7	"	"	1.55	3.20	3.21	20.4 ₅
CR8	4.99	"	"	2.89	2.90	20.4 ₁

^a The ring sizes are given with the accuracy $\pm 0.03 mm$.

^b The j_m values are obtained in the self-field (remanent state) after the long-continued dwell, $t_{dw} = 30 min$.

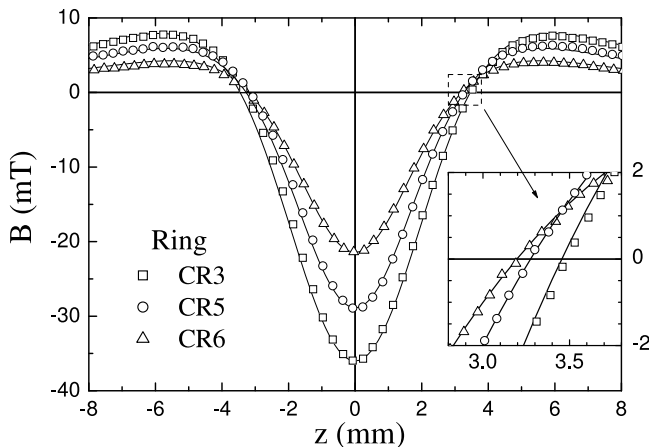


FIG. 6: The axial profiles $B(r=0, z)$ of the remanent flux density (open points) measured at $T = 77.3\text{ K}$ along the axis of the cut rings (see details in Table I) and their approximations (solid curves) given by Eq. (13). Inset magnifies the area around the points $B(z_0) = 0$.

reveals a certain difference. One can notice that the genuine value z_0 (estimated as the half-distance between the points wherein the experimental curve intersects the X -axis) in high rings is usually a bit smaller than z_0 predicted by Eq. (11). This feature is accompanied by the obvious tendency for j_m to decrease (from the top surface to the bottom one) and may readily be explained by the growth-related inhomogeneities of the MT material^{28,29}.

Actually, during a growth the top-seeded MT crystal expands due to a motion of different habitus planes, viz., (100) , $(\bar{1}00)$, (010) , $(0\bar{1}0)$ and $(00\bar{1})$ ²⁸. The growth conditions in the so called a -growth sectors (GS), which appear due to a movement of the former four planes, are different from these in the c -GS, grown on the plane $(00\bar{1})$. In particular, the volume fraction of the Y_2BaCuO_5 inclusions inside the a -GSs considerably exceeds that in the c -GS. Since these inclusions are well-known as effective pinning centers, the critical current density j_m inside the c -GS has to be much smaller than that in a -GSs, i.e. nearby the crystal surface (see Fig. 7). At our growth temperature ($T = 988^\circ\text{C}$) the height of the c -GS is approximately a half of its base²⁹. So, high rings ($2L \geq R_i$) do consist of the superconducting material with different j_m . Grinding the ring bottom, we gradually deleted a part with a

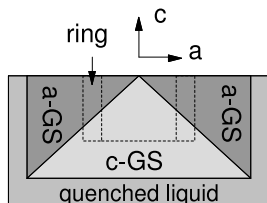


FIG. 7: The central cross-section of the typical MT YBCO crystal. Note that high rings can cross the boundary between the a - and c -sectors grown on different habitus planes, respectively, (100) and $(00\bar{1})$.

worse j_m . One has also to mention that the j_m values in Table I are averaged over the whole height $2L$. A genuine ratio of the current density in the a -GSs and that in the c -GS may roughly be estimated as a factor of 2.0 ± 0.2 .

We also tried to estimate the radial inhomogeneities $j_m(r)$ nearby the top surface of the MT crystals. For this purpose, we removed a certain portion of superconducting material from the outer periphery of the cut ring CR7 (see Table I), but revealed (at least, at the distances $r = 3 \dots 6\text{ mm}$ from the seeding point) no apparent changes.

This brief survey to the growth-induced structure of MT crystals scarcely seems redundant. At first, it confirms a validity of our results. It also gives a better understanding of why we used for further studies only the rings which satisfied the condition $R_i > 2L$ (see Table II). Meantime, it should not eclipse the main, to our opinion, conclusion of this section: the proposed method well predicts the “magic position”, z_0 , where the magnetic flux is free of the intragrain contribution, B_m .

B. Entire rings in the remanent state

In this section we shall report experimental data for entire rings which consist of the a -twisted subgrains. Such subgrains are formed due to mechanical stresses which the YBCO skeleton undergoes when the growth front engulfs the Y_2BaCuO_5 inclusions. These stresses result in dislocations which, unfortunately, have a destructive tendency to amalgamate into the GBs²⁸. As these stresses accrue during the growth, the mis-orientation angle between the neighboring subgrains (which are usually elongated along the growth direction, i.e. along either the a - or the c -axis) gradually increases with a distance from the seeding point²⁸. This angle, for large enough samples, can exceed the critical limit when the GB turns into the weak link^{30,31,32}. Having an opportunity to determine whether this limit is approached or not, we grew few extra-large ($52 \times 52 \times 25\text{ mm}$) MT crystals and cut entire rings from their various parts. So, aside from standard ring parameters (i.e. the inner R_i and the outer R_o radii as well as the full-height, $2L$), we shall hereafter introduce one more, viz., the distance X between the seed and the center of the ring (see Table II). When prepared, each ring was carefully inspected with a view to avoid the cracks which could reduce the effective cross-section $S = (R_o - R_i)2L$ and influence, thereby, on the current distribution inside a ring.

In order to estimate a distribution of the currents flowing in entire rings at the remanent state, we duplicated the procedure described in Section III. Fig. 8a presents the profile $B(r=0, z)$ measured along the axis of the ring ER1 (see Table II). One can, certainly, fit the whole profile $B(r=0, z)$ by selecting appropriate parameters j_m and f in Eq. (7). The best fit is obtained at $j_m = 19.63\text{ kA/cm}^2$ and $j_w = 14.08\text{ kA/cm}^2$ (solid

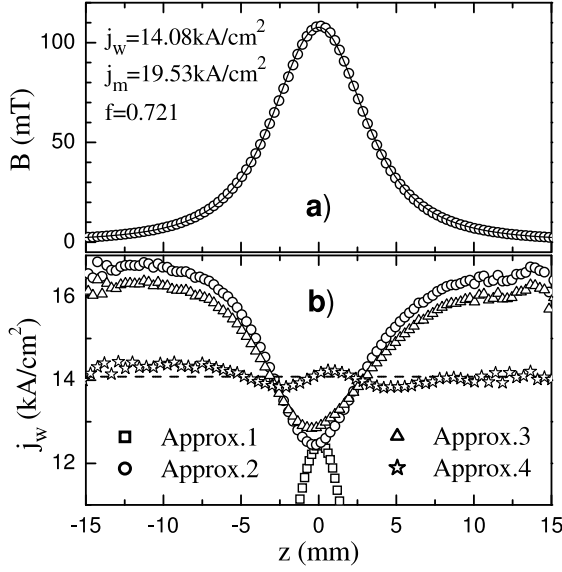


FIG. 8: a) Variation of the remanent flux density $B(r=0, z)$ along the axis of the ring ER1 ($T = 77.3\text{ K}$, $t_{dw} = 30\text{ min}$) and the results of the fitting procedure (solid line). b) The intergrain current densities j_w calculated from these data within various approximations (see details in the text).

line in Fig. 8a). There exists, through, an opportunity to determine the inter- and intragrain currents separately. By substituting the flux densities $B(r=0, \pm z_0)$ into Eq. (12), one obtains quite similar results, $j_w = 14.0$ and 13.9 kA/cm^2 for the points $+z_0$ and $-z_0$, respectively. Estimation of the intragrain current density j_m seems a bit more complicated. Accepting j_w to be the average value 13.95 kA/cm^2 , one can use Eq. (8) to restore the flux density $B_w(r=0, z)$ at arbitrary distance z (say, in the ring center, $z=0$). Then, by deducting this value $B_w(0, 0)$ from the experimental one $B(0, 0)$, one can extract the intragrain flux component, $B_m(0, 0)$. Finally, one has to adjust the parameter f (or $j_m = j_w/f$) in Eq. (9) so to approach the same remainder, $B_m(0, 0)$. Following this procedure, we obtained $f = 0.704$ and $j_m = j_w/f = 19.82\text{ kA/cm}^2$. The latter is in a reasonable agreement both with the

TABLE II: The parameters of entire rings (ER) studied in this work.

Ring No.	R_o	R_i	$2L$	X	z_0	j_w^a	j_m^a	f^a
	mm					kA/cm ²		
ER1	5.00	2.90	2.60	0	2.97	13.9 ₅	19.8 ₂	0.70 ₄
ER2	3.80	2.15	2.00	9	2.24	16.0 ₂	29.4 ₃	0.54 ₄
ER3	7.43	2.30	2.20	0	3.29	19.0 ₂	23.6 ₃	0.80 ₅
ER4	6.00	2.18	3.60	19	3.15	4.6 ₃	10.4 ₁	0.44 ₁

^a The values are calculated by using the “two-point” method from the $B(r=0, z)$ data measured in the remanent state after the long-continued dwell, $t_{dw} = 30\text{ min}$.

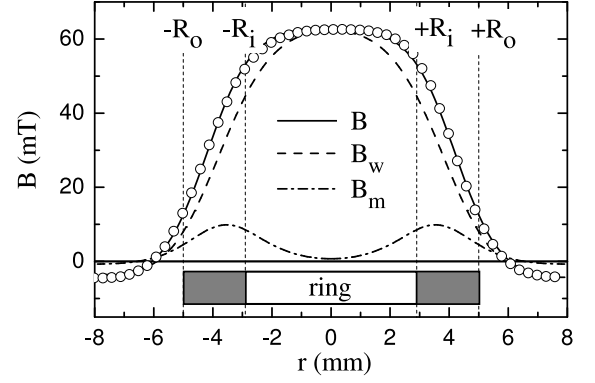


FIG. 9: The radial profile $B^{exp}(r)$ of the remanent flux density measured at $z = 3\text{ mm}$ above the center of the ring ER1 and its theoretical approximation $B^{calc}(r)$ obtained by adjusting parameters j_m and j_w . The best fit values $j_m = 22.3\text{ kA/cm}^2$ and $j_w = 14.05\text{ kA/cm}^2$ ($f = 0.63$) were used to calculate the profiles $B_w(r)$ and $B_m(r)$. Note that since the distance z is close to $z_0 = 2.97\text{ mm}$, $B_m(r=0) \approx 0$.

previous estimate (19.63 kA/cm^2) and with the values ($\approx 20.4\text{ kA/cm}^2$) reported for the cut rings which also were carved from the central part of MT YBCO sample (see Table I). Similar procedure was applied to the other rings, the results are included in Table II. Let us, through, postpone their discussion till the next chapter.

Since any innovation assuredly needs in a careful comparison with the conventional methods, we paid a special attention to this task. At first, we considered those techniques (see, for example, Refs. 9,10,14)

$$B = \begin{cases} I_w/[2R], & \text{Approx. 1} \\ I_w/[2(R^2 + z^2)^{1.5}], & \text{Approx. 2} \\ j_w \Phi(L, z, R_o, R_i), & \text{Approx. 3} \end{cases} \quad (14)$$

which neglect the intragrain flux component B_m . Using each of the mentioned approximations, we calculated the intergrain current densities $j_w = I_w/[2L(R_o - R_i)]$ from the same experimental profile $B(r=0, z)$ and plotted these data in Fig. 8b. It is worth to underline an evident similarity of the curves obtained within the Approx. 2 and 3 with those presented in Fig. 3b. Their deviation from nearly constant value j_w , which corresponds to the case when the intragrain currents are taken into account (Approx. 4 in Fig. 8b), make these methods suitable only for rough estimates even for relatively homogeneous rings like ER1 ($f \approx 0.7$).

Then, we studied the same ring by the approach which is kin to that described in Ref. 10. Briefly, the radial profile $B(r, z = \text{Const})$ in the remanent state ($T = 77.3\text{ K}$, $t_{dw} = 30\text{ min}$) was measured and fitted by adjusting two parameters, j_w and j_m . The obtained data and their fit well agree one with another (see Fig. 9). One has also to mention that a shape of the intergrain flux component $B_w(r)$ noticeably differs from a shape of the experimental curve, $B(r)$. This example once more demonstrates how important is the flux correction due to the intragrain

currents. However, yet more important, at the moment, is a reasonable agreement between the best fit parameters, $j_w = 14.05 \text{ kA/cm}^2$ and $j_m = 22.3 \text{ kA/cm}^2$, and their values estimated by the “two-point” method.

Concluding this section, we would like to emphasize the following. In order to know j_w and j_m , one no longer requires to scan the magnetic flux. Both values may, with a proper accuracy, be determined from *two* experimental data, e.g., $B(z_0)$ and $B(0)$. In contrast to any scanning techniques, this “two-point” method is quite applicable in a wide range of magnetic fields and/or temperatures. This also has no evident restrictions for a time to start the measurements. Realizing these benefits, we used this approach for further studies.

C. Rings in external magnetic fields

Heretofore, we acquiesced to the Bean model which presumes that the critical current density remains independent of the external magnetic field, H . Meantime, H is well-known to reduce j_w . This reduction, in turn, can essentially worsen, say, a performance of superconducting devices constructed from the welded grains. It is, therefore, vitally important to control the intergrain current I_w which flow through the weak link immersed in strong magnetic fields. Another task on which we are going to focus an attention is a penetration of a magnetic flux into the rings. This process was recently shown²² to be accompanied by a highly non-uniform current distribution. Although our approach describes mostly rings in the full-magnetized state, this allowed to shed some light onto this phenomenon.

Since a behaviour of the rings enumerated in Table II gradually changed from the most homogeneous case, ER3 ($f = 0.80$), to the most inhomogeneous one, ER4 ($f = 0.44$), these were the samples which we selected for an illustration.

Fig. 10 presents the B vs H dependencies obtained at various heights, $z = 0$ and $z = 3.3 \text{ mm} \approx z_0$, above the center of the ring ER3 a) before and b) after we introduced therein the radial slit. Let us primarily discuss the flux penetration into a bore ($z = 0$) of the zero-field-cooled (zfc) ring in the non-magnetized, virgin state (open symbols).

Fig. 10a shows that the entire ring shields ($B = 0$) its bore³³ by generating the circular current I_w which, at first, exactly compensates $\mu_0 H$. However, I_w is limited by its critical value. Thus, the field H_p , when the currents are no longer enough for full screening ($B > 0$), may be used to estimate the critical current density j_w .

Penetration of the magnetic flux into a bore ($z = 0$) of the cut rings seems absolutely different. Since there are no circular currents ($I_w = B_w = 0$), the flux density is defined merely by the intragrain flux component, B_m . For this reason, the initial curve $B(z = 0)$ in Fig. 10b deviates from zero as soon as $H > 0$. One can also observe that the initial slope $dB/\mu_0 dH$ exceeds unity. In other words,

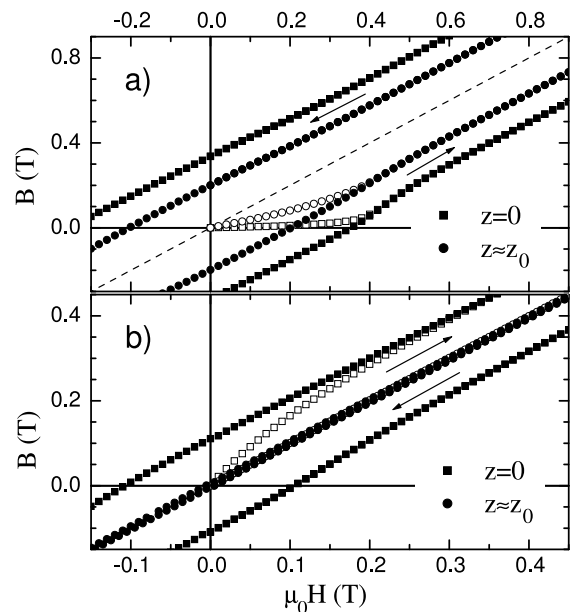


FIG. 10: The B vs H dependencies ($T = 77.3 \text{ K}$, the sweep rate 0.5 T/min) for the ring ER3 a) without and b) with the radial slit. The curves were measured at various heights, $z = 0$ and $z_0 \approx 3.3 \text{ mm}$, above the ring center.

the $B(z = 0)$ loop in the cut rings and that in the entire rings have opposite widths $\Delta B = B - \mu_0 H$ (Fig. 10). This behavior is reminiscent of the opposite components, $B_m(z = 0) < 0$ and $B_w(z = 0) > 0$, of the remanent flux presented in Fig. 3. The B_m vs z dependencies on Figs. 3 and 6 also explain why the loop $B(H)$ in the cut rings shrinks into the straight line $B = \mu_0 H$ as z increases up to z_0 (see the respective curve in Fig. 10b) and, then, expands again with the negative width, $\Delta B(z > z_0) < 0$.

Extremely interesting anomalies (see Fig. 11) accompany the flux penetration into a bore ($z = 0$) of the ring ER4, where the weakest link is really weak ($f = 0.44$) as compared with the rest of the ring material. In particular, the curve of the magnetic flux density $B(z = 0)$ at the initial field branch (open squares) approaches the full-magnetized loop (solid squares) from outside, i.e. there exist the field range ($0.08 \text{ T} \leq \mu_0 H \lesssim 0.5 \text{ T}$) wherein the partially magnetized ring more effectively screens its bore than that in the full-magnetized state. Similar anomalies are also observed nearby the field reversal. Fig. 11 shows these effects at $\mu_0 H = 1.25 \text{ T}$, solid lines on the right side of Fig. 11 correspond to the loop reversed at a bit higher magnetic field, $\mu_0 H = 1.5 \text{ T}$. Since these anomalies almost disappear at the height $z = z_0$ (circles), one can preliminary conclude that these are induced by changes in a distribution of the *intragrain* currents which correspond to the concentric, counterrotating current loops mentioned in Ref. 22.

To test this suggestion, we realized the following experiments. The samples were zfc-cooled down to $T = 77.3 \text{ K}$ and magnetized at this temperature in a certain field, H . When a field was switched off, the remanent flux den-

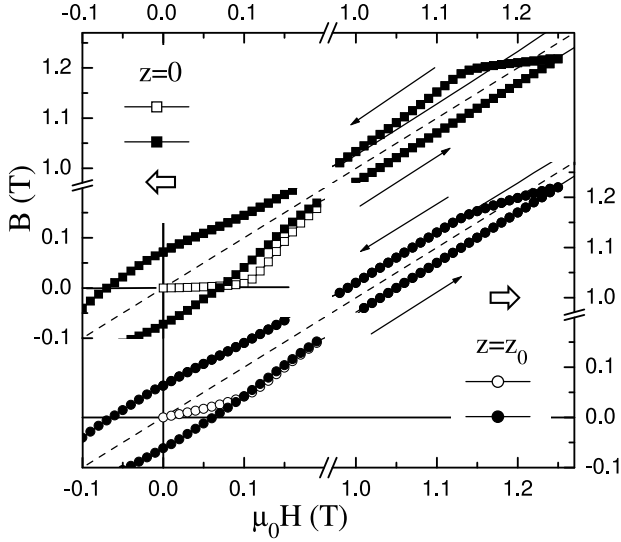


FIG. 11: The B vs H dependencies ($T = 77.3$ K, the sweep rate 0.5 T/min) for the ring ER4. The data are measured at various heights, $z = 0$ and $z_0 \approx 3.15$ mm, above the ring center. Solid lines (on the right side) correspond to the loops re-magnetized at higher magnetic field, $\mu_0 H = 1.5$ T. Note that the $B(z = 0)$ anomalies during the field penetration (on the initial branch, $\mu_0 H \approx 0.12$ T, as well as on the descending field branch, nearby the field reversal) are absent at the height $z = z_0$.

sity was registered (after $t_{dw} = 10$ s) at various heights above the ring center, $z = 0$, z_0 and $z > z_0$. We repeated this procedure at gradually increasing H until the remanent flux density B approached its saturation. The obtained B vs $\mu_0 H$ dependencies (normalized to the B values at $\mu_0 H = 2$ T which well exceeds the full-penetration field) are presented in Fig. 12. One can see that the flux density in the center of the weakly coupled ring ER4 (open circles) does exhibit a well-discernible maximum at $\mu_0 H = 0.18$ T. Similar maximum was already observed in polycrystalline YBCO rings by Mohamed and Jung⁴. However, the concept of the Josephson vortex flow, which they invoked to unravel this phenomenon, can scarcely explain why the maximum totally disappears at larger distances, $z = z_0$ and $z > z_0$ (respectively, squares and up triangles in Fig. 12).

To our opinion, both the maximum $B(z = 0)$ in Fig. 12 and the $B(z = 0)$ anomalies in Fig. 11 are of the same origin. Their reason becomes nearly obvious owing to the normalization trick used in Fig. 12. These phenomena occur since the full-penetration field $\mu_0 H_p \approx 0.5$ T (which is necessary to induce the whole currents) in the weakly coupled ring ER4 is much larger than the field $\mu_0 H_w \approx 0.2$ T wherein the intergrain current reaches its critical limit, $j_w 2L(R_o - R_i)$ (squares in Fig. 11). So, a further growth of magnetic field ($H_w \leq H \lesssim H_p$) can generate merely the intragrain currents. Since the intragrain flux component B_m reverses its sign at the height $z = z_0$ (see, for example, Figs. 3, 6 or 10b), the increase of its amplitude has to result in an additional increment

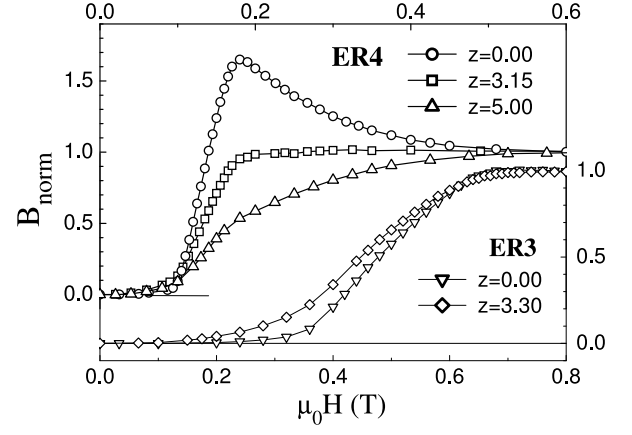


FIG. 12: The remanent flux density B vs the magnetic field $\mu_0 H$ at which the zfc-rings, ER3 (right and bottom axes) and ER4 (left and top axes), were magnetized ($T = 77.3$ K). The curves correspond to various distances, $z = 0$, $z = z_0$ and $z > z_0$ (given in mm), where the flux density was registered after the short dwell, $t_{dw} = 10$ s. Each curve is normalized to the full-penetration value obtained at $\mu_0 H = 2$ T.

of the net flux density B measured at $z > z_0$ and, what we are going to prove, in its reduction when $z < z_0$. In other words, we believe that these anomalies become visible owing to demagnetizing effects. One more argument in favor of this scenario is that the ratio $H_w/H_p \approx 0.4$ does appear very close to the parameter $f = 0.44$. The same scenario is quite relevant for explication of the flux anomaly after the field reversal.

Generally, a certain decrease of the remanent flux could also be explained by the sample heating due to viscous forces that exert on moving flux lines. Yet, to attain the difference of 65% shown in Fig. 12, one usually needs in the pulsed fields when the sweep rate is in a few orders of magnitude faster³⁴ than that (0.5 T/min) used in our experiments. Another argument, which completely rejects a hypothesis of the sample heating, is an absence of *any* $B(z = 0)$ anomalies for more homogeneous ring ER3 ($f = 0.80$) which was measured at the same experimental conditions (Fig. 12). This absence may readily be explained by the following reasons. At first, the critical value of the intergrain current $I_w \sim f$ linearly grows with f and so is the flux component B_w which I_w produces. Since the intragrain current $I_m \sim (1 - f^2)$ has an opposite tendency, the ratio B_m/B_w rapidly decreases as $f \rightarrow 1$. Finally, the larger is f , the closer become the fields H_w and H_p where, respectively, the inter- and the intragrain currents are saturated. Hence, the larger half ($\sim f$) of the intragrain flux component B_m appears *simultaneously* with the intergrain one ($H < H_w$) and only a small portion, $\sim (1 - f)$, does in the range $H_w \leq H \lesssim H_p$ where the B_m changes are not compensated by the B_w growth.

Thus, the closer is f to unity, the less pronounced have to be the $B(z = 0)$ anomalies during the flux penetration. The studies of other rings (enumerated in Table II) confirm this statement. In particular, a difference between the maximum of the remanent flux $B(z = 0)$ and

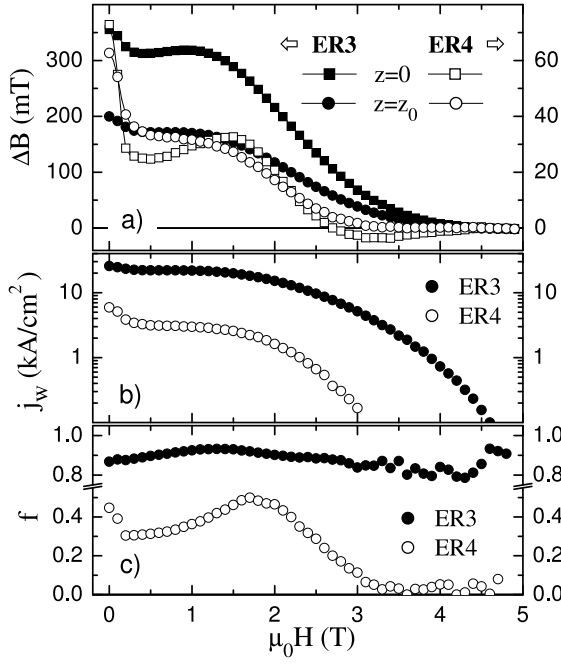


FIG. 13: a) The half-width $\Delta B(H)$ of the flux density loops shown in Figs. 10a and 11. The field dependencies b) $j_w(H)$ and c) $f(H)$ are calculated from the $\Delta B(H)$ data.

its saturation value for the ring ER2 was registered to be 3.6% ($H_w/H_p = 0.6 \approx 0.54 = f$). For the rings ER1 and ER3 with $f = 0.70$ and $f = 0.80$, respectively, this value did not exceed the experimental error ($\approx 0.3\%$). On the other hand, one can conclude, be the conclusion ever so amazing, that the remanent flux density $B(z < z_0)$ of weakly coupled rings ($f \rightarrow 0$) may totally vanish or even become negative (note, for example, a negative remanence of $\approx -0.1 T$ in the center of the cut ring ER3 shown in Fig. 10b) as the magnetizing field ascends.

Let us yet come back to an estimation of the intergrain and the intragrain current densities in external magnetic fields. As mentioned above, our approach requires removing the constant background $\mu_0 H$ from the experimental data, $B(z = 0)$ and $B(z = z_0)$, in the full-magnetized state (full points in Figs. 10a and 11). This task may conveniently be resolved by calculating the half-difference between the descending, B_\downarrow , and the ascending, B_\uparrow , field branches

$$\Delta B(H) = [B_\downarrow(H) - B_\uparrow(H)]/2. \quad (15)$$

Then, by applying the “two-point” method to each pair of the points, $\Delta B(H)|_{z=0}$ and $\Delta B(H)|_{z=z_0}$ presented in Fig. 13a, we restored the sought $j_w(H)$ and $j_m(H)$ dependencies as well as their ratio $f(H)$ which also was found to depend on H . Moreover, the weaker is the link, the more sensitive this appeared to external magnetic fields (see Fig. 13c). In particular, in contrast to the sample ER3 which values f cluster around 0.9, the curve $f(H)$ in the ring ER4 exhibits two well-defined maxima. Their origin can be attributed to the strongly coupled channels in

GBs with a low misorientation angle^{30,31,32}. According to Dimos³⁰ and Chisholm³¹, small magnetic fields *partially* decouple a weak link, i.e. there exists a secondary, non-weak-linked component of the intergrain conduction. Such channels of relatively undisturbed crystal lattice (i.e. microbridges of the intrinsic, intragranular material which occupy only a small area of the GB surface) were directly confirmed by the transmission electron microscopy of the 10° -bicrystal YBCO film³². Following this multifilamentary model, one can identify the saddle point between two mentioned maxima as the field which decouples the weakest link, but still does not influence onto the other weak links restricting the intragrain current I_m given by Eq. (3). So, a further increase of field reduces mostly the intragrain current density, $j_m(H)$, and, hence, results in the second peak of the $f(H)$ dependence. More interesting is that the same sequence seems valid for high fields H_{irr} which totally decouples weak links by breaking their strongly coupled channels. Fig. 13c shows that this decoupling first happens with the weakest link $\mu_0 H_{irr} \approx 3.3 T$ and, then, with the rest of weak links ($\approx 4.6 T$) in the ring ER4. In other words, within the range $3.3 T \lesssim \mu_0 H \lesssim 4.6 T$ there is already no transport current ($f = 0$), but the intragrain currents, which result in $B_m < 0$, still continue to flow. It is the reason why the half-width $\Delta B(H)|_{z=0}$ (open squares in Fig. 13a) alters its sign. To our knowledge, only this type of measurements opens up an opportunity to see this high-field phenomenon.

Finalizing this section, one has to mention some discrepancies between the parameters $f(H = 0)$ extracted from the magnetization cycle data (Fig. 13c) and those which were registered after a long dwell (see Table II). Comparing these values, we took cognizance of a weak tendency for f to decrease with a time. This question, through, is worthy of a separate discussion.

D. Dissipation of the magnetic flux

It is well known that the thermoactivated vortices ($T > 0$) can leave the pinning centers under the Lorentz force³⁵

$$F_L = V \frac{B}{\mu_0} \frac{dB}{dr}. \quad (16)$$

Such motion of the vortex lines is equivalent to a resistance to a current and responsible for the power dissipation. For this reason, we were not surprised that the absolute values of the inter- and the intragrain current densities were found to decrease during a dwell. Meanwhile, their ratio f was also suspected to depend on a time. If this tendency does exist, the flux depinning processes may noticeably falsified a genuine ability f of weak links to transmit the current. It is therefore very important to know to which extent can we rely on the previous data obtained by the scanning Hall-sensor magnetometry^{8,9,10,11,12,13,14,15} which *a-priori* requires a long-continued dwell.

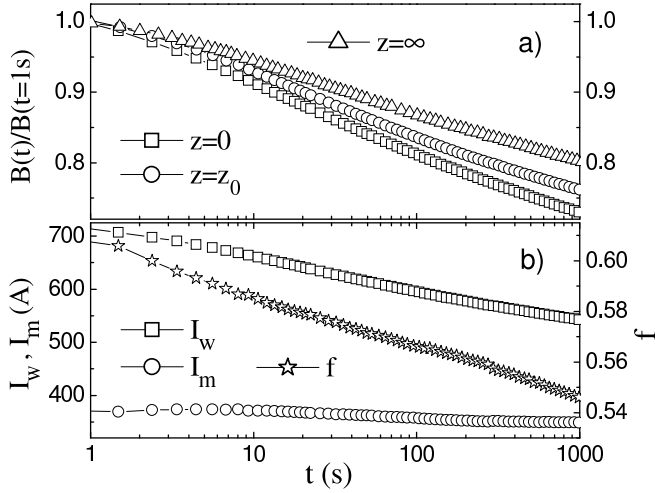


FIG. 14: a) Dissipation of the remanent flux density $B(t)$ measured at various heights z above the center of the ring ER2 ($T = 77.3 K$). The curve $z = \infty$ corresponds to the time changes of the remanent magnetic moment, m . b) The inter- and intragrain currents, I_w and I_m , as well as the parameter $f = j_w/j_m$ which are restored from these data.

At first, we more carefully explored the inter- and the intragrain flux losses and their influence on the current distribution. Fig. 14a shows the time dependencies of the remanent flux density measured at various heights, $z = 0$, z_0 and ∞ above the center of the ring ER2. These curves (normalized, for convenience, to their values $B_0 = B(t = 1 s)$) neatly indicate that the relative dissipation rate

$$S = -\frac{1}{B_0} \frac{dB(t)}{d \log t} \quad (17)$$

gradually decreases with a distance z from the sample. This decrease does prove that the intergrain current I_w is dissipated faster than the intragrain one, I_m . Using the “two-point” procedure, we confirmed this qualitative conclusion by the numerical values I_w and I_m (Fig. 14b). The intergrain current decay S was determined to be 8.2% per the time decade, whereas S for the intragrain current did not exceed 2%. From these values we estimated the effective heights $E = k_B T / S$ of the energy barrier which has to be overpassed by the flux vortex to leave the pinning center. These heights were found to be 0.081 eV and 0.341 eV, respectively. Consequently, every time decade reduced the parameter f on 0.021.

There may be several reasons which explain this phenomenon. The most evident one is that the intragrain current loop does not cross the weakest link where the largest losses are expected. One can also attribute this effect to the Lorentz force (16) which, in accordance to the radial distribution $B(r)$ (see Fig. 2a), more effectively stimulates a motion of the flux vortices trapped nearby the inner periphery ($R_c < r < R_i$) of the ring. This question will be the subject of next studies.

Whatever are the genuine reasons, these do result in the spatial re-distribution ($f \neq \text{Const}$) of the currents

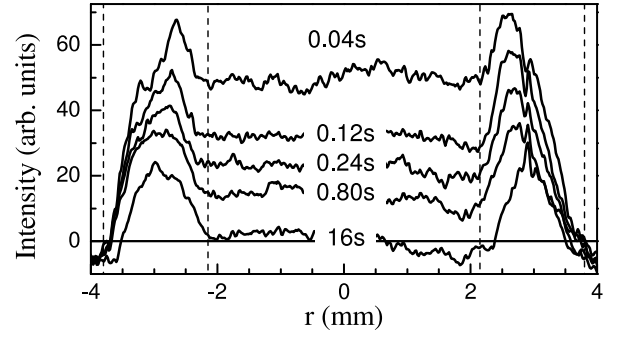


FIG. 15: Radial profiles of the remanent flux density $B(r, z)$ on the surface $z = \pm L$ of the ring ER2 at various dwell times (in seconds). The data were obtained by the magneto-optical imaging technique ($T = 81 K$).

during a dwell. This re-distribution passes the faster, the faster is the flux creep itself. One can conclude that at low temperatures and small magnetic fields, slow experimental methods still may give a reasonable approximation for the parameter f describing the current limiting properties of the weak link. Otherwise, the long-continued dwell is absolutely inadmissible and so, unfortunately, is the *scanning* Hall-sensor method, which provides another way to discern between the inter- and the intragrain currents¹⁰. In order to visualize how appallingly large may become an error just after a few seconds of dwell, we investigated the remanent flux creep in same ring ER2 at higher temperature, $T = 81 K$. In view of extremely sharp decay, we were caused to use the magneto-optical image technique²⁷ which allowed to register the flux changes much faster than other methods. So, the ring was cooled down to 81 K, isothermally magnetized and, then, a magnetic field was rapidly (during a delay 0.04 s between neighboring image frames) switched off. Fig. 15 clearly shows that the flux inside the ring bore $|r| < 2.15 \text{ mm}$ (dashed lines), i.e. that which is induced by the intergrain (circular) current I_w , rapidly decreases. In other words, a genuine value f (defined mostly by the GB microstructure^{30,31,32} which is independent of a temperature) may be obtained only at $t \rightarrow 0$. Slow methods ($t \gg 1 s$) will falsely report that the weakest link in this ring can transmit nearly no current, i.e. $f \approx 0$.

V. SUMMARY

We explored the inter- and the intragrain currents flowing in bulk MT YBCO samples containing weak links.

To perform these studies, we developed a simple, reliable and non-destructive method which allows to discern between these types of current. In particular, we showed that, if a sample has a shape of a ring with finite sizes, the intragrain current (because of demagnetizing effects) gives an alternating-sign contribution B_m to the net flux density B , viz., B_m is negative nearby the ring center and positive at large distances. We also considered the

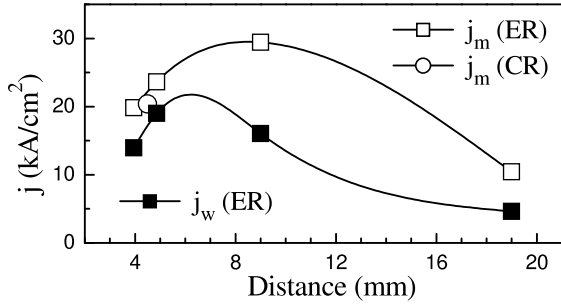


FIG. 16: Distributions of the inter- and the intragrain current densities inside the MT YBCO crystal vs the distance from the seeding point. The data are compiled from measurements of both the entire rings (ER) and the cut ones (CR).

points $z = \pm z_0$, wherein the ring axis ($r = 0$) intersects the border ($B_m = 0$) between these areas, and demonstrated that the distance z_0 appears almost independent of the current distribution. Hence, positioning the Hall sensor at the height $\pm z_0$ above (or below) the ring center, one can measure the “pure” intergrain flux component, B_w , and estimate the intergrain (circular) current which produces B_w . This, the so-called “one-point” method seems very promising for characterization of a quality of superconducting welds. In this case, the numerical calculations of the distance z_0 may optionally be replaced by its direct measurement preceding to the welding procedure. The same idea may, in future, be extended for less exotic sample shapes, for example, for the finite-size slabs.

By measuring the flux density $B(r = 0, z)$ in one more point $z \neq z_0$, one can also restore the intragrain current, I_m . We showed that it is the current which is responsible for very unusual phenomena registered nearby the center ($r = 0, z = 0$) of weakly coupled rings ($f < 0.5$). In particular, we observed (see Figs. 11 and 12) that, being in partially penetrated state, such rings screen their bores more effectively than those after the full-flux-penetration. Similar situation was registered after the field reversal at

relatively high fields (Fig. 11). We also revealed, to the first blush, absolutely irregular situation when, owing to a destruction of the strongly coupled channels^{30,31,32} in the weakest link, magnetic fields $H \geq H_{irr}$ result in a negative screening of the ring bore (Fig. 13a). The dependence of the flux dissipation rate S on a distance z from the ring (Fig. 14a) could also be scarcely explicable unless the intragrain current I_m is taken into account. These effects are merely the first items in a large list of somewhat “strange” effects (both already published and still waiting for publication³⁶) in the finite-size superconducting rings and/or hollow cylinders. We believe that, by presenting the method which allows to estimate I_m , this work opens new perspectives to reveal and to explain other items.

Concluding the paper, we would like to touch on the superconducting welding again. Unless the welding techniques give totally reproducible quality of joints, one has to minimize their number by welding the bulk MT crystals which are as large as possible. Their sizes, through, are severely restricted because of a degradation of the superconducting properties from the seeding point toward the crystal rims (see Fig. 16). There exist, therefore, an optimum size, i.e. the size at which the rims of welded parts may transmit the same density of transport current as that which can flow across the future joint. Since, at present, the best joints are reported to carry the currents with a density of $\approx 10 \text{ kA/cm}^2$, we believe that the welding technology should be developed mostly for joining of relatively large, $25 \times 25 \text{ mm}$ MT YBCO blocks.

Acknowledgments

This work was supported by the German BMBF under the Project 13N6854A3 and by the Russian Foundation for Basic Research (Project 02-02-17062). One of the authors (A.B.S.) would like to thank R. Hieregeist for useful discussions.

* The author to whom a correspondence should be addressed; On leave from Institute for Magnetism, Kiev, Ukraine; Electronic address: surzhenko@ipht-jena.de

¹ P. Leiderer and R. Feile, Z. Phys. B **70**, 141 (1988).

² M. A.-K. Mohamed and J. Jung, Phys. Rev. B **44**, 4512 (1991).

³ J. Jung and I. Isaac, Phys. Rev. B **48**, 7526 (1993).

⁴ H. Darhmaoui and J. Jung, Phys. Rev. B **53**, 14621 (1996).

⁵ S. Jin, T. H. Tiefel, R. C. Sherwood, M. E. Davis, R. B. van Dover, G. W. Kammlott, R. Fastnacht and H. D. Keith, Appl. Phys. Lett. **52**, 2074 (1988).

⁶ M. J. Sturm, Z. A. Chaudury and S. A. Akbar, Mater. Lett. **12**, 316 (1991); K. Salama and V. Selvamanickam, J. Appl. Phys. **60**(7), 898 (1992).

⁷ D. Shi, Appl. Phys. Lett. **66**, 2573 (1995).

⁸ Ph. Vanderbemden, A. D. Bradley, R. A. Doyle, W. Lo,

D. M. Astill, D. A. Cardwell and A. M. Campbell, Physica C **302**, 257 (1998).

⁹ H. Zheng, M. Jiang, R. Nikolova, U. Welp, A. P. Paulikas, Yi Huang, G. W. Crabtree, B. W. Veal and H. Klaus, Physica C **322**, 1 (1999).

¹⁰ H. Zheng, H. Claus, L. Chen, A. P. Paulikas, B. W. Veal, B. Olsson, A. Koshelev, J. Hull and G. W. Crabtree, Physica C **350**, 17 (2001).

¹¹ T. Prikhna, W. Gawalek, V. Moshchil, A. Surzhenko, A. Kordyuk, D. Litzkendorf, S. Dub, V. Melnikov, A. Plyushchay, N. Sergienko, A. Koval, S. Bokoch and T. Habisreuther, Physica C **354**, 333 (2001).

¹² M. P. Delamare, H. Walter, B. Bringmann, A. Leenders and H. C. Freyhardt, Physica C **329**, 160 (2000).

¹³ C. Harnois, G. Desgardin and X. Chaud, Supercond. Sci. Technol. **14**, 708 (2001).

- ¹⁴ T. Puig, P. Rodriguez Jr., A. E. Carillo, X. Obradors, H. Zheng, U. Welp, L. Chen, H. Claus, B. W. Veal and G. W. Crabtree, *Physica C* **363**, 75 (2001).
- ¹⁵ J. Yoshioka, K. Iida, T. Negichi, N. Sakai, K. Noto and M. Murakami, *Supercond. Sci. Technol.* **15**, 712 (2002).
- ¹⁶ J. G. Noudem, E. S. Reddy, M. Tarka, M. Noe and G. J. Schmitz, *Supercond. Sci. Technol.* **14**, 363 (2001).
- ¹⁷ H. Walter, Ch. Jooss, F. Sandiumenge, B. Bringmann, M. P. Delamare, A. Leenders and H. C. Freyhardt, *Europhys. Lett.* **55**(1), 100 (2001).
- ¹⁸ H. Claus, U. Welp, H. Zheng, L. Chen, A. P. Paulikas, B. W. Veal, K. E. Gray and G. W. Crabtree, *Phys. Rev. B* **64**, 144507 (2001).
- ¹⁹ A. A. Kordyuk, V. V. Nemoshkalenko, A. I. Plyushchay, T. A. Prikhna and W. Gawalek, *Supercond. Sci. Technol.* **14**, L41 (2001).
- ²⁰ M. Kambara, N. Hari Babu, D. A. Cardwell and A. M. Campbell, *Physica C* **372–376**, 1155 (2002).
- ²¹ M. Murakami, *Supercond. Sci. Technol.* **13**, 448 (2000).
- ²² M. Pannetier, F. C. Klaassen, R. J. Wijngaarden, M. Welling, K. Heeck, J. M. Huijbregtse, B. Dam and R. Griessen, *Phys. Rev. B* **64**, 144505 (2001).
- ²³ A. B. Surzhenko, M. Zeisberger, T. Habisreuther, D. Litzkendorf and W. Gawalek, *Supercond. Sci. Technol.* **15**, 1353 (2002).
- ²⁴ C. D. Dewhurst, Wai Lo, Y. H. Shi and D. A. Cardwell, *Mater. Sci. Eng.* **B53**, 169 (1998).
- ²⁵ D. Litzkendorf, T. Habisreuther, M. Wu, T. Straßer, M. Zeisberger, W. Gawalek, M. Helbig and P. Gönert, *Mater. Sci. Eng.* **B53**, 75 (1998).
- ²⁶ Th. Klupsch, Th. Straßer, T. Habisreuther, W. Gawalek, S. Gruss, H. May, R. Palka, and F. J. Mora Serrano, *J. Appl. Phys.* **82**, 3035 (1997).
- ²⁷ L. S. Uspenskaya, V. K. Vlasko-Vlasov, V. I. Nikitenko, and T. H. Johansen, *Phys. Rev. B* **56**, 11979 (1997).
- ²⁸ P. Diko, *Supercond. Sci. Technol.* **13**, 1202 (2000).
- ²⁹ A. B. Surzhenko, S. Schauroth, M. Zeisberger, T. Habisreuther, D. Litzkendorf and W. Gawalek, *Physica C* **372–376**, 1212 (2002).
- ³⁰ D. Dimos, P. Chaudhari, J. Mannhart and F. K. LeGoues, *Phys. Rev. Lett.* **61**, 219 (1988); D. Dimos, P. Chaudhari and J. Mannhart, *Phys. Rev. B* **41**, 4038 (1990).
- ³¹ M. F. Chisholm and S. J. Pennycook, *Nature* **351**, 47 (1991).
- ³² N. F. Heinig, R. D. Redwing, I. Fei Tsu, A. Gurevich, J. E. Nordman, S. E. Babcock and D. C. Larbalestier, *Appl. Phys. Lett.* **69**(4), 577 (1996).
- ³³ Similar behavior in the type-I superconductors was described by W. Buckel, *Superconductivity: Fundamentals and Applications* (VCH, Weinheim, 1991) p.173.
- ³⁴ A. B. Surzhenko, S. Schauroth, M. Zeisberger, T. Habisreuther, D. Litzkendorf and W. Gawalek, *Supercond. Sci. Technol.* **14**, 770 (2001).
- ³⁵ see, for example, A. Gurevich and E. H. Brandt, *Phys. Rev. Lett.* **73**, 178 (1994).
- ³⁶ L. S. Uspenskaya *et al.*, *to be published*.
- ³⁷ Numerical methods (e.g., the bisectional search) determine the roots $\pm z_0$ of Eq.(11) to any desired accuracy. For this reason, we desisted from attempts to reduce Eq. (11) into an absolute form $z_0 = f(R_i, R_o, L)$ which can be obtained by introducing further restrictions for the ring geometry.
- ³⁸ Owing to a finite height of real rings, a requirement for the ratio R_o/R_i is actually yet less stringent.